Oxidation of NiCr and NiCrMo Alloys at Low Temperatures

Cameron Volders,* Gopalakrishnan Ramalingam,* Valentina Angelici Avincola,* Iradwikanari Waluyo, Adrian Hunt,** and Petra Reinke‡,***

Oxidation of Ni-Cr and Ni-Cr-Mo was studied in operando with near ambient pressure x-ray photoelectron spectroscopy in the Cabrera-Mott regime. The oxidation temperature was 200°C—a severely diffusion-limited regime. The near-surface alloy is Cr-enriched after the reduction of native oxide in vacuum, and especially so for Ni-15Cr-6Mo. Mo-cations are integrated into the oxide and Mo(VI) dominates at the surface. The surface chemistry-driven promotion of chromia by Mo predicted by theory is negated by the limited surface diffusion of reactants. Preoxidation processing is proposed to control the oxide properties for the use of Ni-Cr superalloys at low temperatures.

KEY WORDS: form B. (operando), form B. (XPS), mat A. (Ni), mat A. (Ni-Cr), prop C. (oxidation), prop C. (surface science)

INTRODUCTION

NiCr alloys are highly coveted for various technical applications as they exhibit a combination of superior corrosion resistance and high-temperature strength.[1-4] These superalloys are used in a number of challenging environments including the nuclear fuel industry, the petrochemical industry, as well as for marine applications.[5-7] The Ni base provides the mechanical strength for the system while Cr establishes the corrosion/oxidation resistance upon the formation of a passive Cr_2O_3 film.[1,3-4,8] A critical concentration of 10 wt% to 15 wt% Cr is necessary for the Cr_2O_3 layer to protect the underlying alloy from further degradation. The properties of NiCr alloys are further enhanced through the addition of minor alloying elements (MAE) such as Mo and W.[9-14] For example, alloying with Mo reduces catastrophic breakdown events, namely localized crevice corrosion, thereby improving overall corrosion resistance.[8,10-11,14-16] In high-temperature alloys, molybdenum is added to enhance mechanical strength by solid solution hardening.[17] However, Mo forms volatile oxides which can rupture the passive chromium oxide that is formed in these alloys.[18-19] The spallation becomes relevant at temperatures greater than 600°C and severely degrades the operational lifetime of components.

The mechanisms which are responsible for the beneficial impact of MAEs on the quality of the oxide layer remain a subject of discussion in the literature.[13] From an aqueous corrosion viewpoint, the solute vacancy interaction model suggests Mo has a direct effect on the transport of point defects and influences oxide film growth.[14] The model argues Mo^{4+} and Mo^{6+} cations become incorporated into Cr_2O_3 films as substitutional defects and electrostatically interact with cation vacancies and reduce their mobility. The decreased mobility slows the formation of cation vacancy condensates which have been proposed to initiate pit formation.[14,16] To date, most of the work on MAEs and their role in enhancing oxide layer stability[13-15] has focused on processes in the oxide and mostly neglected the initial alloy-oxygen interaction, and their role in oxide growth. Recent studies give an atomic scale view into the oxidation process on the reaction of O_2 with Ni-Cr alloys using operando transmission electron microscopy, and scanning tunneling microscopy and spectroscopy (STM/STS).[20-27] In those references the competition between Ni and Cr oxidation is illustrated at temperatures, where the oxidation process is kinetically limited and below the volatilization temperature of Mo-oxides. Atomic scale imaging using STM and operando studies with near ambient pressure-x-ray photoelectron spectroscopy (NAP-XPS) have been extended to compositionally more complex alloys such as Ni-Cr-W and stainless steels.[22-23,25,28] It was shown experimentally that the addition of W to Ni-Cr alloys enhances chromia formation for oxidation at T > 400°C. The experimental results are supported by density functional theory (DFT) calculations, which identify the favorable site for O-adsorption at W-Cr bridge sites.[22] This agrees with the DFT study by Samin and Taylor[29] who investigated oxygen adsorption for Ni-Cr-Mo alloys and reported an increased O adsorption energy also for Cr adjacent to Mo atoms. The oxygen adsorption energy was recently introduced as a descriptor to predict competition between oxidation processes on compositionally complex alloy surfaces.[30]

Discrepancies exist in the literature on the effect of Mo addition when alloys are oxidized at temperatures below 500°C. Greeff, et al.,[31] observed no influence of Mo on the oxidation of Fe-9Cr-1Mo steel after 1,000 L oxidation at 157°C to 758°C. However, Mathieu and Landolt[32] report at 384°C that the oxidation rate of Fe-24Cr-11Mo alloy is lower than the corresponding alloy with Mo. It was observed that Mo accumulates at the oxide/metal interface in hexavalent and metallic states and this barrier layer slows down the oxidation rate. Montemor, et al.,[33] also observed the presence of Mo at the interface and in the internal chromium oxide layer on stainless steels oxidized at 250°C to 450°C, whereas the chromium oxide contribution

---

Submitted for publication: June 29, 2023. Revised and accepted: September 14, 2023. Preprint available online: September 14, 2023, https://doi.org/10.5006/4400.

‡ Corresponding author. E-mail: pr6e@virginia.edu.
* Department of Materials Science and Engineering, University of Virginia, Charlottesville, Virginia 22904.
** National Synchrotron Light Source II, Brookhaven National Laboratory, Upton, New York 11973.

ISSN 0010-9312 (print), 1938-159X (online)

increased with the addition of Mo to stainless steel. All literature reports for low T oxidation study thicker oxide scales, whereas the work presented here focuses on the Cabrera-Mott regime with oxide thicknesses in and below the 10 nm range.

The current work observes oxide evolution for different NiCr alloys including Ni-5Cr, Ni-15Cr, Ni-30Cr, and Ni-15Cr-6Mo by wt% using NAP-XPS. The oxidation temperature is 200°C and the diffusion of reactants from bulk to surface is therefore suppressed.[34-36] Previous work on the nucleation and growth of NiO islands on Ni-5Cr(100) surfaces at 300°C combined STM experiments and modeling based on the Johnson-Mehl-Avrami-Kolmogorov equation as a framework.[37] The capture radius for adsorbed oxygen atoms is only about 0.4 nm from the edge of an oxide island which confirms the locality of this process and the limits posed on the diffusion length. The oxide islands do not yet display the characteristic NiO structure which is clearly visible at higher oxidation temperatures. The island structure is closer to a diffusion-limited aggregation growth mode where reduced ad-atom mobility prevents reaching the thermodynamically favored crystalline structure.[20-21,38]

In our present study, the oxidation reaction was probed in real time—in operando—by using NAP-XPS. The oxide growth was performed at $p(O_2) = 0.0133$ mbar and this positions our work in the Cabrera-Mott regime. The near-surface composition of the alloy is replicated in the oxide composition and Mo is integrated predominantly as Mo(IV) and Mo(VI) at the alloy/gas interface. Alloying with Mo increases the near-surface Cr inventory determined by the reduction of the native oxide by annealing prior to the oxidation experiment.

EXPERIMENTAL PROCEDURE

The NAP-XPS experiments were performed at Brookhaven National Laboratory (BNL) using the ambient pressure photoelectron spectroscopy (APPES) endstation at the in situ and operando soft x-ray spectroscopy (IOS/23-ID-2) beamline at the National Synchrotron Light Source II (NSLS-II). Details about the beamline and endstation are described elsewhere.[39] The NiCr samples were cast into rectangular prisms, cold-worked to between 22% and 24% strain, and then recrystallized at 900°C for 1 h, with the exception of the NiCrMo alloy, which was recrystallized at 1,300°C. The samples were cast by John Perepezko, University of Wisconsin-Madison.[22] Energy dispersive spectroscopy (EDS) was used to confirm sample homogeneity and composition. The samples were then polished to a mirror finish and cut into suitable dimensions for the XPS sample holder.

The alloys were introduced into the ultra-high vacuum (UHV) chamber of the APPES endstation (base pressure $\sim p(O_2) = 1.3 \times 10^{-9}$ mbar) and annealed at $T = 800°C$ to remove the native oxide layer, which was confirmed by measuring the $Ni2p_{3/2}$, $Cr2p_{3/2}$, Mo3d, and O1s core levels. The Ni-15Cr-6Mo wt% sample was annealed at $T = 600°C$ to avoid the formation of volatile MoO_3.[40] The oxygen concentration was <0.5% for all alloys prior to starting the oxidation experiments. The sample temperature was then decreased to the oxidation temperature of 200°C and spectra of the $Ni2p_{3/2}$, $Cr2p_{3/2}$, and Mo3d core levels were measured again immediately prior to oxidation. Figure 1 summarizes alloy compositions measured by EDS (after alloy casting) and by XPS at 200°C just before oxidation was started. Figure 1 includes spectra of the $Ni2p_{3/2}$ and $Cr2p_{3/2}$ core levels for the Ni-15wt%Cr alloy before oxidation. All compositions, unless otherwise stated, are given in wt% and written as Ni-5Cr, Ni-15Cr, Ni-30Cr, and Ni-15Cr-6Mo.

The alloys were oxidized at 200°C and $p(O_2) = 0.01$ Torr for up to 5,000 s with high-purity (99.997%) molecular oxygen. Core level spectra for $Ni2p_{3/2}$, $Cr2p_{3/2}$, Mo3d, and O1s were recorded during the oxidation process in an operando mode. A photon energy of $h\nu = 1,120$ eV and a pass energy of 10 eV were used for all measurements. A step size of 0.1 eV was used for the $Ni2p_{3/2}$ core level spectra and 0.05 eV for $Cr2p_{3/2}$ and Mo3d. The resolution of the XPS at BNL varies between 0.1 eV and 0.2 eV depending on the photon energy with higher energies trending toward 0.2 eV. The acquisition times for each core level were between 95 s and 200 s with slight adjustments throughout the measurements for modification of binding energy range or operating pressure as needed. All figures including data points with respect to time for specific elements use the time recorded at the start of measuring the specific core level. This can be seen, for example, in Figure 2 where the data points for the different elements are slightly shifted with respect to each other accounting for their true start time.

The spectra were analyzed with the fitting software, KolXPD† (XPS analysis software kolibri.net). All spectra were fit with a Shirley background, a Doniach-Sunjic function for the Ni(0), Cr(0), and Mo(0) metal peaks to account for their inherent asymmetry,[41-46] and all oxide peaks were fit using a Voigt function. The multiplet splitting for Ni2p and Cr2p oxide peaks is described by Biesinger, et al.,[41-45] and a constrained fit is used which follows the published reference spectra. The $Ni2p_{1/2}$ core level was not included in our measurements, and preference was given to achieving shorter data acquisition time to more fully capture the oxidation process. A detailed description of the fit process is included in the Supplemental Materials S1. The $Au4f_{7/2}$ peak of an Au foil mounted on the sample holder was positioned at a binding energy of 84.0 eV for energy calibration. The core levels were corrected by their respective cross sections[47] for all calculations of composition.

RESULTS

The spectra and composition of the pristine alloys are summarized in Figure 1, which includes the bulk and surface composition of the alloys as measured by EDS and XPS at 800°C (600°C), and 200°C immediately prior to the start of the oxidation experiment. Figures 1(b) and (c) show the core level spectra of the pristine alloy surface for Ni-15Cr as a representative example. The $Ni2p_{3/2}$ and $Cr2p_{3/2}$ core levels are positioned at 853.8 eV and 574.4 eV, respectively, and the satellite accompanying $Ni2p_{3/2}$ is readily apparent on the high binding energy side. The oxygen concentration on the surface is <1% and no oxide contributions are detected in the Ni and Cr core level spectra. In Figure 1(c), the XPS measurements reveal a Cr-enriched alloy surface for all alloys after oxide reduction, which is retained to a lesser degree after cooling down to 200°C with the exception of Ni-15Cr. This alloy shows a near-surface Cr depletion compared to the bulk composition, which is tentatively attributed to the presence of more rapid diffusion pathways defined by microstructure, or thermal history during and after casting. Future experiments using temperature-programmed reduction of native oxides will clarify the interplay between native oxide reduction and microstructure, which ultimately defines the near-surface composition.[48-52]

The panels in Figures 2(a) through (d) summarize the evolution of oxide and metal signals with exposure time for all alloys. Ni(0), Cr(0), Mo(0), NiO, Cr_2O_3, and MoO_3 signal

---

† Trade name.

Composition Measured by EDS	Composition Measured by XPS					
	Ni at%		Cr at%		Mo at%	
Sample	**800°C Anneal**	**200°C pre-ox.**	**800°C Anneal**	**200°C pre-ox.**	**600°C Anneal**	**200°C pre-ox.**
Ni-5Cr (wt%) Ni-5.61Cr (at%)	89.8	91.0	10.2	9.0	N/A	N/A
Ni-15Cr (wt%) Ni-16.61Cr (at%)	75.8	90.6	24.2	9.4	N/A	N/A
Ni-30Cr (wt%) Ni-32.6Cr (at%)	32.7	45.6	67.3	54.4	N/A	N/A
	600°C Anneal		**600°C Anneal**			
Ni-15Cr-6Mo (wt%) Ni-17.0Cr-3.68Mo (at%)	54.6	62.3	38.0	33.2	7.4	4.5

(a)

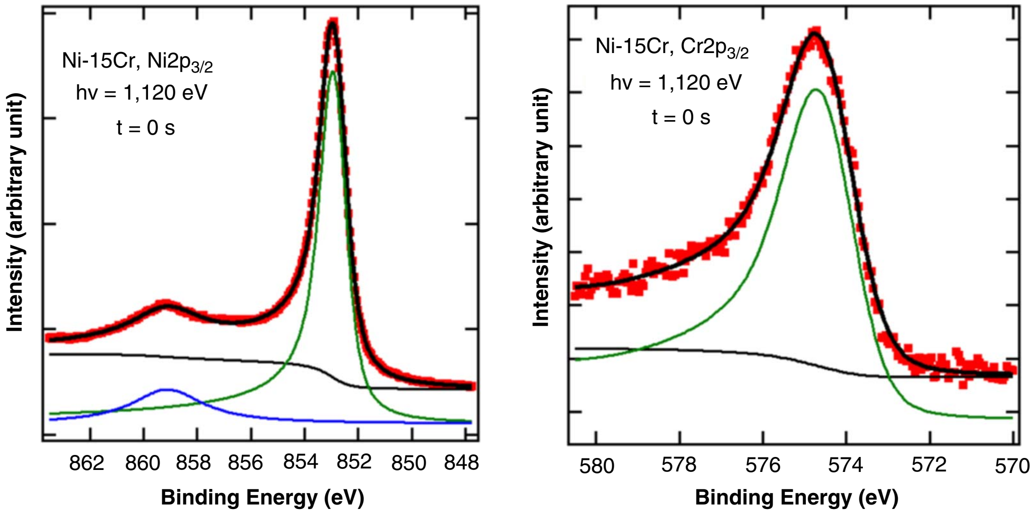

(b) (c)

FIGURE 1. *(a) Tabulated compositions for the bulk alloy measured with EDS, and the surface composition of the alloy after annealing and prior to the oxidation experiment measured with XPS. Due to the sample heterogeneity, the XPS composition cannot be corrected for mean free path variation between Ni and Cr core levels. Representative core level spectra of the clean alloy Ni-15Cr: (b) Ni2p$_{3/2}$ and (c) Cr2p$_{3/2}$.*

intensities were plotted as a fraction of the total signal intensity, which was the sum over all core level signals after correction for the respective photoemission cross section.[53] The general trend is similar for all alloys with a rapid increase in the oxide signal in the first 360 s of the oxidation, and concomitant reduction in the alloy signal. The oxide layer grows rapidly and is almost certainly a closed layer within the first few oxidation steps as evidenced by the rapid decay of the alloy signal. An oxidation step in this context is understood as one cycle through the measurement of all core levels. However, the decay of the alloy signal at longer oxidation times is shallower than expected for layer-by-layer growth which is in agreement with the morphological complexity of the oxide. The present experiment covers the transition from an alloy surface-dominated reaction regime—the pre-Cabrera-Mott regime—into the Cabrera-Mott regime, where transport through the oxide drives growth. This is in contrast to our earlier work described in Volders, et al.,[22] where the alloy surface reactions were isolated through the use of a lower p(O_2). The oxide compositions are resolved in Figure 3, and the evolution of the alloy signal is described in Figure 5.

Figure 3(a) illustrates the interplay between NiO and chromia contributions, and Figures 3(b) and (c) are representative fits for Ni2p$_{3/2}$ and Cr2p$_{3/2}$ core levels close to the endpoint of the oxidation experiment. The Cr-oxide is identified as chromia by core level fitting, and detailed information about the fit process is given in the Supplemental Material S1. The chromia contributions at the first oxidation step are about 12% for Ni-5Cr and Ni-15Cr, and significantly larger for Ni-30Cr and Ni-15Cr-Mo with 53% and 34%, respectively. The error bar in the composition calculation is about 5%. The Mo-oxide contribution is not included in this graph and will be discussed separately. The chromia signal is reduced by 10% to 15% over the course of the oxidation time which can be linked to NiO overgrowing chromia islands formed early in the oxidation.

Oxidation of Cr is thermodynamically favorable,[2-4,54] and the dominance of NiO at low oxidation temperatures is attributed to a lower nucleation barrier due to epitaxial lattice matching at the alloy/oxide interface and sluggish bulk diffusion of Cr, and consequently reduced reactant supply.[34-36,55] Earlier work on NiCr oxidation with STM also illustrates the inherent

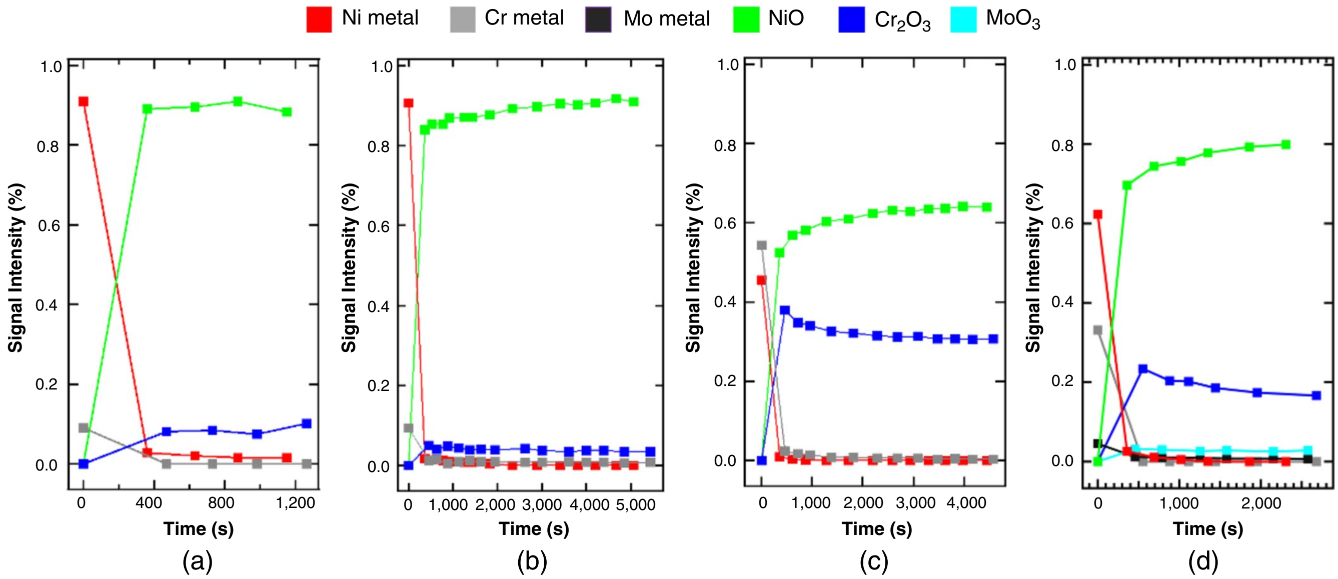

FIGURE 2. *Composition for all samples as a function of oxidation time at T = 200°C, $p(O_2)$ = 0.01 Torr. Ni, Cr, Mo metal, and corresponding oxide contributions are obtained from a fit of the core levels. The sum of all contributions is set to 1, and the signal intensity reflects the change in the relative contributions of the constituents over time. Note that the time scales differ between oxidation experiments. (a) Ni-5Cr, (b) Ni-15Cr, (c) Ni-30Cr, and (d) Ni-15Cr-5Mo.*

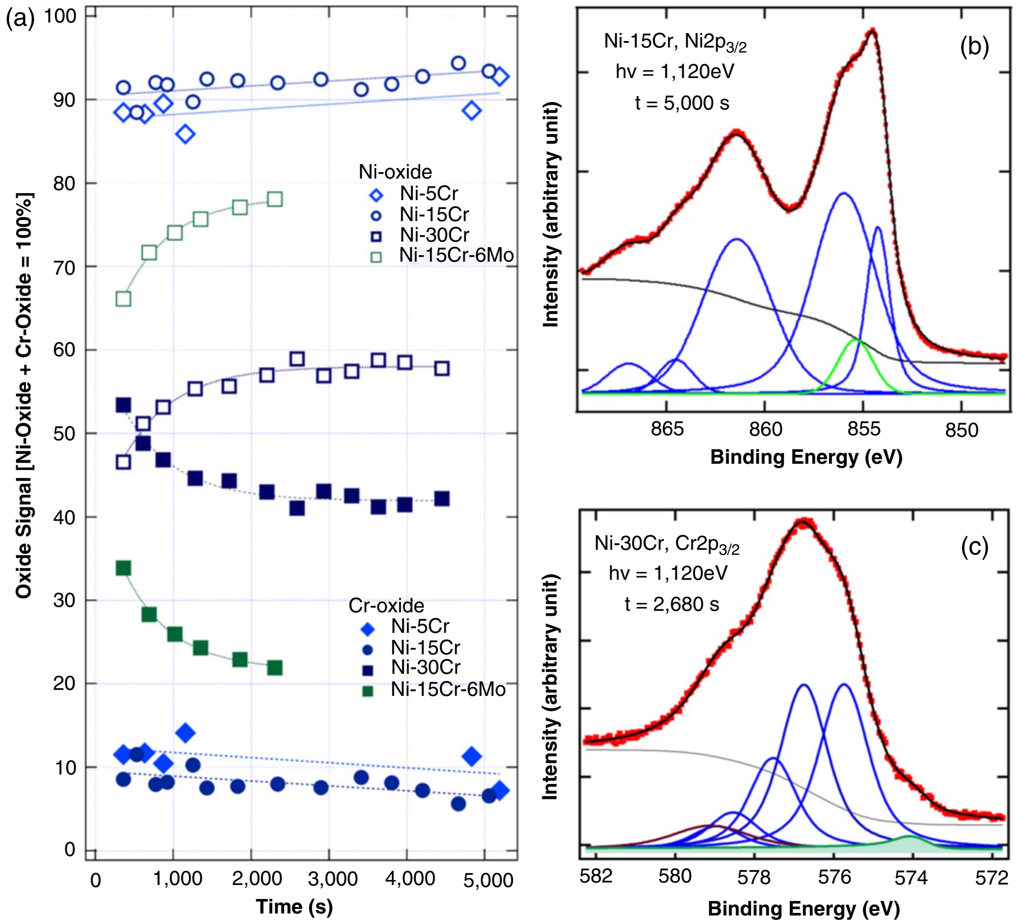

FIGURE 3. *(a) Evolution of the oxide layer composition with Ni-oxide and Cr-oxide contributions for all alloys. The measurement of Ni-5Cr was interrupted for technical reasons. Examples of core level fits (b) $Ni2p_{3/2}$ and (c) $Cr2p_{3/2}$. Red symbols: measured spectra, black line: envelope of the fit, broken black line: Shirley background. (b) Ni $2p_{3/2}$: blue lines—NiO multiplet, green line—Ni^{3+} or defect peak, no alloy contribution. (c) $Cr2p_{3/2}$: blue lines—Cr_2O_3 multiplet, green line—Cr(0), and dark line marking a low-intensity peak on the high binding energy—not assigned.*

morphological complexity which is superimposed on the chemical complexity seen in XPS: NiO tends to grow in a layer-by-layer growth mode driven by interfacial, epitaxial alignment between Ni and NiO lattices, while chromia prefers an island growth mode with small clusters or nodules with high aspect ratios.[20-21]

Analysis of the Ni2p$_{3/2}$ spectra shown in Figure 3(b) revealed an additional component at a binding energy of 855.0 eV, which is tentatively assigned to Ni(III) ions. Fit examples with and without this component are included in the Supplemental Material S1, and it is evident that the associated spectra cannot be described by including spinel $NiCr_2O_4$ multiplets (Supplemental Material in Volders, et al.,[22] for details). Figure 3(c) illustrates the excellent quality of the chromia phase for Ni-15Cr-6Mo, which is indistinguishable from the pristine chromia reference described in the literature. The high quality of chromia on the ternary alloy enhances the protective function of the oxide layer.

Figure 4 isolates the 855.0 eV binding energy peak introduced in the description of the Ni2p core level and marked in green in Figure 3(b). It should be noted that Ni(III) is fully represented as a multiplet structure as described in Biesinger, et al.[42-43] The fit quality as expressed by the residuals did not change with the use of a multiplet compared to the use of a single peak to represent Ni(III) which is included in the figure. This is due to the overlap of the more intense multiplet peaks from NiO and Ni(0) with those of Ni(III). No hydroxide contributions, which are positioned at binding energies exceeding approximately 530.5 eV are present in any O1s core level. NiOOH can therefore be excluded as the origin of the Ni(III) peak. The nature of the component at 855.0 eV has been debated in the literature, and proposed interpretations include $NiOO_{ads}$ or NiO_{ads} chemisorbed species,[56] small contributions from $Ni(OH)_2$,[57] the formation of a nonequilibrium Ni_2O_3 structure,[56,58] and surface defects related to excess Ni vacancies.[59-70] The formation of Ni(III) as a means to maintain charge neutrality in a defective NiO crystal is the most widely accepted explanation and can be summarized using the Kröger-Vink notation:

$$2Ni_{Ni}^{x} + \frac{1}{2}O_2(g) \rightarrow 2Ni_{Ni}^{\bullet} + O_O^{X} + V_{Ni^{\bullet}}^{\prime\prime} \tag{1}$$

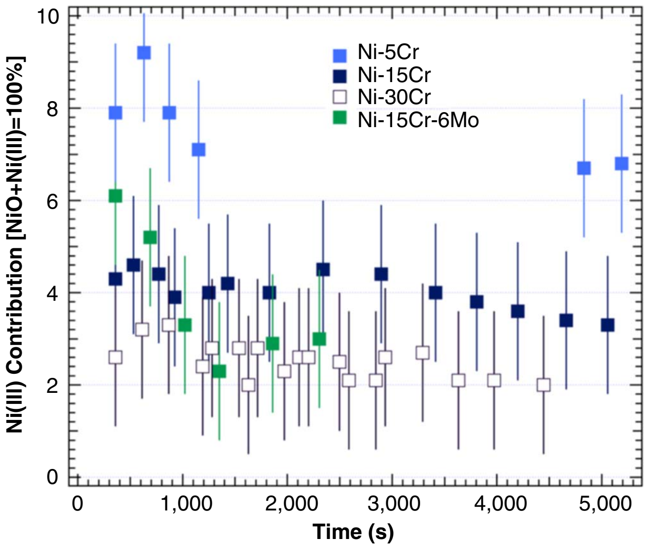

FIGURE 4. *Ni(III) contribution for all alloys as a function of oxidation time. The sum for NiO+Ni(III) is set to 100%. The fit process is described in the Supplemental Material S1.*

The concentration of Ni(III) ions is constant within the error bar throughout the oxidation process, except for two data points for Ni-15Cr-6Mo at the start of the oxidation time, and Ni5Cr. This could indicate a different defect population in this alloy, but a conclusive interpretation would require observing shorter timescales of oxidation not accessible in the present experiment. The overall trend in Ni(III) contribution implies that Ni(III) ions are either distributed in the NiO phases, or at the chromia-NiO grain boundaries and are not unique to the alloy/oxide interface. The associated vacancies might serve as precursors to the formation of Kirkendall voids.[26]

Following the detailed discussion of the oxide layer composition, we will now take a closer look at the attenuation of the metal signal, which includes information about the oxide layer growth mode and the alloy/oxide interface. The alloy signal shown in Figure 5 is the sum of all metals M(0) detected at the respective time step and the graph begins with the first oxidation step at 360 s captured with XPS. The growth of the oxide layer during this initial step (prior to measurement) is rapid and attenuates the alloy signal from 100% to less than 10% as seen in Figure 5. All alloys accumulate an oxide with appreciable thickness reaching nearly the information depth of the photoelectron spectroscopy, which is conventionally defined as 4 × IMFP (inelastic mean free path). The attenuated alloy signal recorded in the first oxidation step is commensurate with an oxide layer thickness of several nanometers. Ni-15Cr-6Mo presents the steepest slope after the first oxidation step and approaches most closely a layer-by-layer growth. Because we are only able to detect the tail end of the decay function it is not possible to extract more quantitative information about the growth mode.

The total metal signal includes only Ni(0) for Ni-5Cr, Ni(0) and Cr(0) for Ni-15Cr, and Ni-30Cr, and Ni(0) and Mo(0) but no Cr(0) for Ni-15Cr-6Mo. The total metal signal as shown in Figure 5 starting at the second and all following oxidation steps, only includes the elements which are detected in their metallic state. This number excludes the oxide (cationic) contributions to the respective core level. For Ni-5Cr, no Cr(0) is detected anymore, and the same holds for Ni-15Cr-6Mo. For the two other alloys, we still can see a Cr(0) signal. For oxidation times >1,500 s, more than 80% of the respective alloy signal is either Cr(0) (Ni-15Cr, Ni-30Cr) or Mo(0) (Ni-15Cr-6Mo) with Ni(0) as a balance to 100%. This is in contrast to oxidation experiments at 500°C, where the alloys were completely depleted in Cr(0) and Mo(0) in the near-interface region.[22] However, if the overlayer (oxide) thickness is close to the photoelectron information depth the element-specific variation in IMFP has to be considered in the interpretation. The imfps in the alloy for hv = 1,120 eV are as follows: Ni2p—0.6 nm, Cr2p—1.0 nm, and Mo3d—1.4 nm. All values were calculated with Quases (Quases-IMFP-TPP2M Ver.3.0[†]) which follows the method described by Tanuma, et al.[71] The IMFP values for oxides are about 10% to 20% larger than for metals.

Once the detection limit is approached for Ni(0), the element with the smallest IMFP, the alloy composition cannot be measured anymore. The detection limit is set here by the ability to separate Ni(0) from the NiO contribution to the core level and is about 1% to 1.5%. Once this limit is reached Cr(0) and Mo(0) with their larger IMFPs and consequently larger intensity will disproportionally contribute to the alloy signal. An experimental solution can be to measure each element with a different

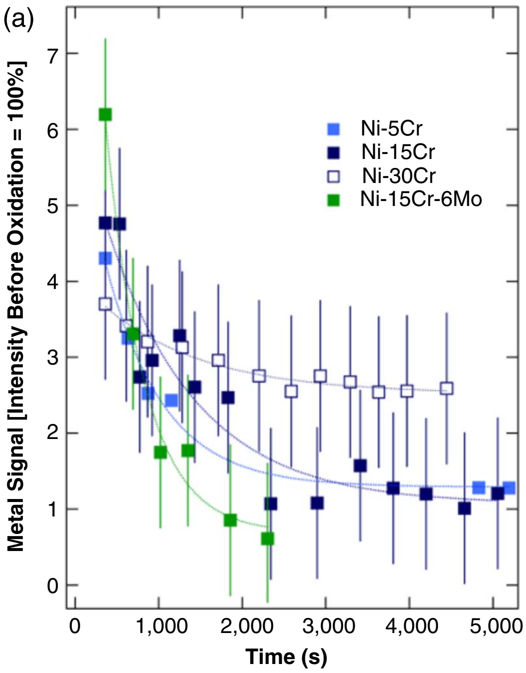

(b)

Metal M(0) Signal Intensity After first Oxidation Step	
Ni-5Cr	4.3±1% [Ni]
Ni-15Cr	4.8±1% [Ni+Cr]
Ni-30Cr	3.7±1% [Ni+Cr]
Ni-15Cr-6Mo	6.1±1% [Ni+Mo]

FIGURE 5. *Attenuation of the metal signal for all alloys after the first oxidation step. (a) Metal signal as a function of oxidation time includes all M(0) contributions—Ni(0) for Ni-5Cr, Ni(0) and Cr(0) for Ni-15Cr and Ni-30Cr, and Ni(0) and Mo(0) for Ni-15Cr-6Mo. Elements not listed were not detected. The error bar reflects the precision of the fit process. (b) Tabulated values of the metal signal at the first oxidation step recorded after 360 s exposure. The initial M(0) concentration is 100%.*

photon energy to adjust all IMFP's to the same value as done in the work by Larsson, et al.,[72] but this comes at the cost of acquisition rate. In conclusion, we can confirm that Cr(0) is present at the alloy/oxide interface for Ni-15Cr and Ni-30Cr, but not for Ni-5Cr and Ni-15Cr-Mo; and Mo(0) is present at the Ni-15Cr-6Mo interface. Quantitative information on the near-interface alloy composition cannot be obtained, and enrichment factors as defined by Castle and Asami cease to be informative.[73] Cr(0) or Mo(0) are not fully depleted at the interface for select alloys which might be explained by a kinetic bottleneck, where transport through the alloy to the interface is more rapid than the oxidation rate.

The evolution of the Mo3d core level for Ni-15Cr-6Mo is shown in Figures 6(a) through (e) at select oxidation times and is the only element, where two oxidation states are recognized. For each spectrum, the Mo3d$_{5/2}$ and Mo3d$_{3/2}$ metal peaks were fit using a Doniach-Sunjic function convoluted with a Gaussian with a 3.2 eV peak separation, and a spin-orbit branching ratio of 1.5. Mo(0)3d$_{5/2}$ is positioned at 228.4 eV, Mo(IV) at 229.9 eV, and Mo(VI) at 232.4 eV, respectively.[56-58] Figure 6(a) is the pristine alloy, and as the oxidation progresses, Mo(VI) and Mo(IV) oxidation states emerge. Figures 6(d) and (e) were measured with lower photon energies to extract a depth distribution of the respective oxidation states. The oxidation was continued to avoid reduction of the surface in UHV, and the process is stopped after a total oxidation time of 3,653 s with a measurement at hν = 500 eV.

The contributions from the various Mo oxidation states are summarized in Figure 7. After 1,500 s the oxide composition remains constant within the error of the measurement. Mo(VI) is the majority component, and Mo(IV) accounts for about 15% at the endpoint of the experiment. The Mo(0) contribution is reduced due to oxide layer growth. Figure 7(b) resolves the depth distribution of the oxidation states: Mo(VI) dominates close to the surface as seen in its higher contribution at lower photon energies, and Mo(0) and Mo(IV) are more prevalent as we probe closer to the alloy/oxide interface. The Mo(0) concentration decreases with reduced photon energy (probe depth) but the concurrent increase in Mo(VI) is steeper and confirms that Mo (VI) is enriched in the surface. The oxidizing environment at the solid/gas interface favors the higher oxidation state. The concentration of Mo(IV) hovers between 5% and 15% with the lower values observed for reduced information depth and thus closer to the solid/gas interface. The availability of two Mo oxidation states allows for a multitude of solid-state reactions with Ni and Cr oxides and defects. The latter is one of the mechanisms which is held responsible for the unique ability of Mo cations to scavenge defects created during crevice, pitting, or another breakdown event.[13]

DISCUSSION

The oxidation of Ni-Cr and Ni-Cr-Mo alloys leads to the formation of a protective layer made of Ni- and Cr-oxides whose contributions are determined by processing parameters and materials characteristics. The relatively low temperature during oxidation used in the present work leads to very slow diffusive processes,[36,74-75] thus throttling reactant supply and favoring somewhat defective oxides over the high-quality crystalline layers seen at higher temperatures. The enrichment of the alloy surface with Cr after the high-temperature reduction of the native oxide, which is summarized in Figure 1, scales with the contribution of chromia to the oxide in the very first oxidation step recorded. The information is summarized in Figure 8 and includes the oxide composition after the first oxidation step, and after 2,500 s when the oxide composition reaches a plateau. The slight decrease in chromia contribution as a function of oxidation time is likely due to a higher growth rate for NiO.

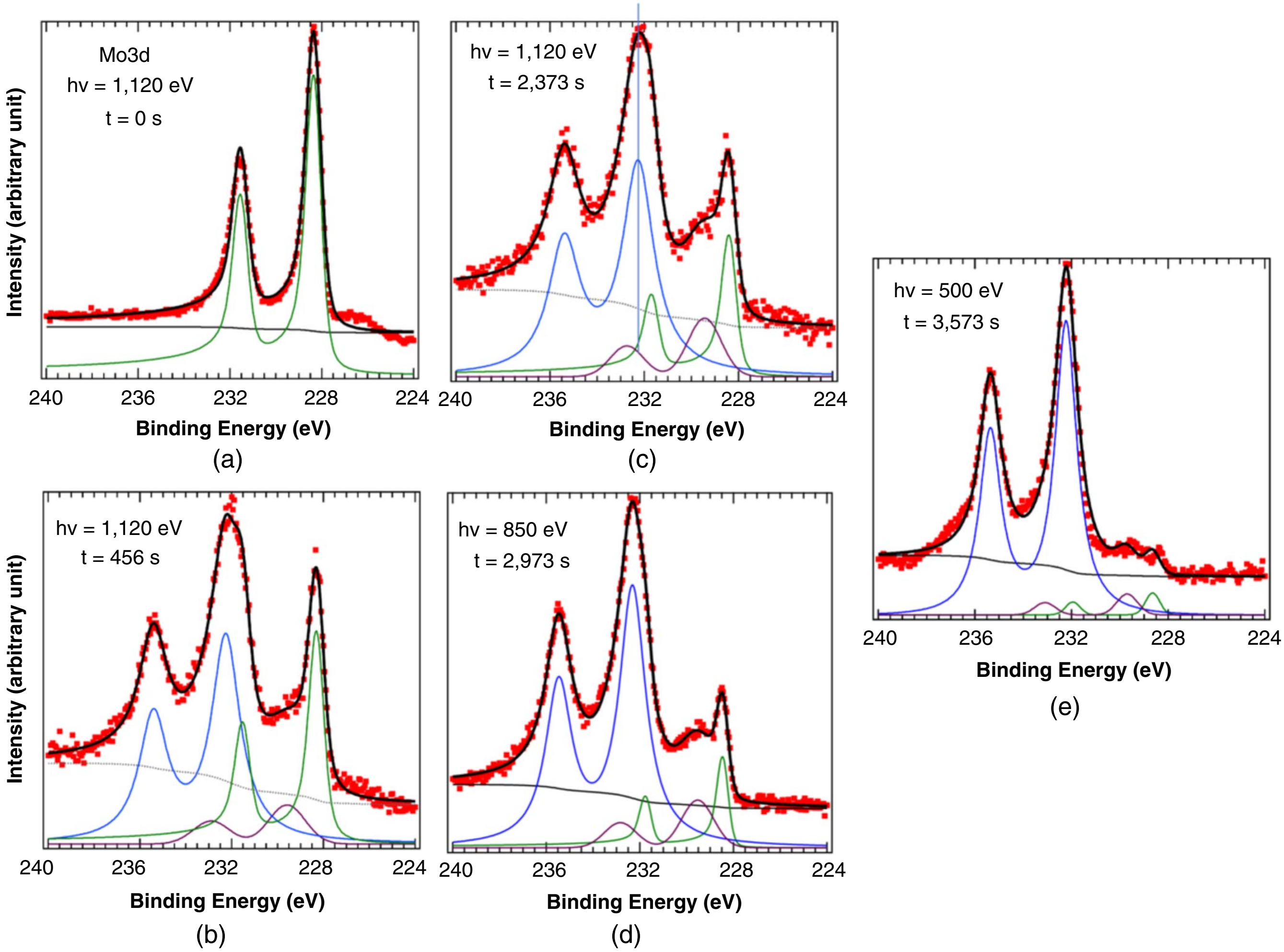

FIGURE 6. *Mo3d core level at select times during the oxidation process. Red symbols: measured spectra, black line: envelope of the fit, thin black line: Shirley background, green lines: Mo(0), blue lines: Mo(VI)—MoO$_3$, and purple lines: Mo(IV)—MoO$_2$. (a) pristine alloy, (b) and (c) M(0) and oxides, (d) photon energy of 850 eV, and (e) photon energy of 500 eV to probe the near-surface region.*

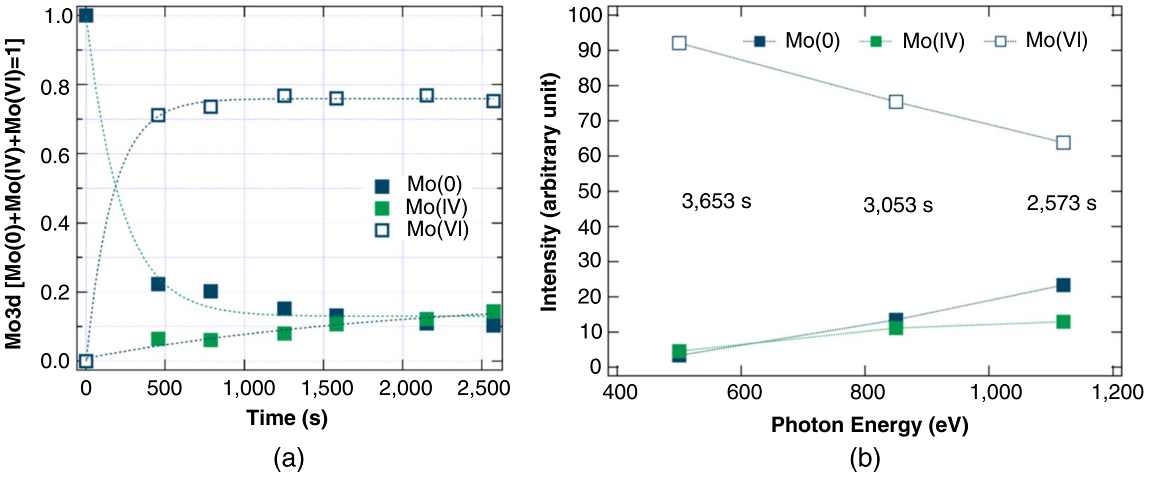

FIGURE 7. *(a) Contributions of different oxidation states to the Mo signal as a function of oxidation time. (b) Oxidation state contributions as a function of photon energy and oxidation time. The variation in photon energy yields a depth profile with 500 eV as the most surface-sensitive measurement. The oxidation time for each measurement is indicated by the numbers on the centerline.*

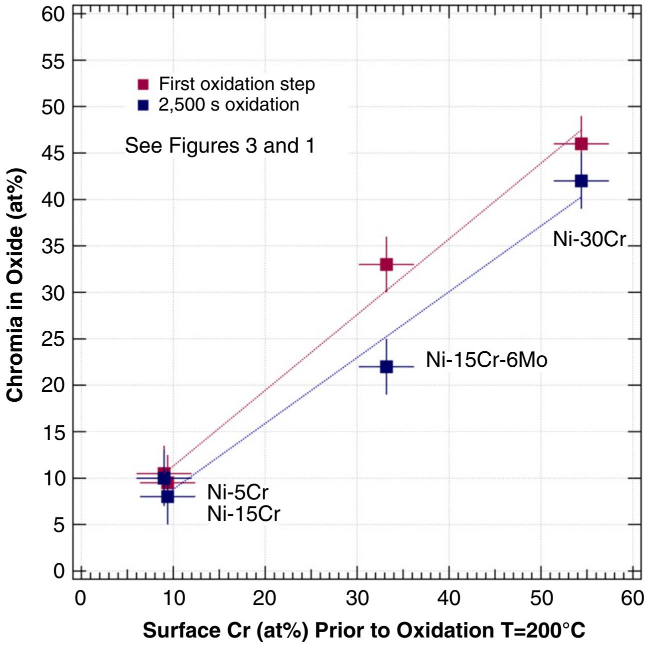

FIGURE 8. *Comparison of surface composition and oxide composition for Cr. The first oxidation step measured at 360 s and the one at 2,500 s are compared, and the data are also presented in Figures 1 and 4.*

The pre-Cabrera-Mott regime which represents the early stages of oxidation, was studied in more detail in our recent publication[22] on the oxidation of Ni-Cr and Ni-Cr-W alloys (T = 400°C and 500°C, $p(O_2) = 10^{-6}$ Torr), where the addition of W favored chromia formation by a large margin. This is explained by preferred O-adsorption at Cr-sites adjacent to W as determined by DFT calculations.[29,76-79] The oxygen adsorption energy was identified as a suitable descriptor for the affinity for oxidation of a specific element and predictions for Ni-Cr-Mo mirror our work on Ni-Cr-W.[29] The favored adsorption sites between (W, Mo) and Cr present a facile pathway to chromia formation.

The direct comparison of the Ni-Cr-W experiments with our present work has to be approached with caution: first, we intentionally target here an oxidation parameter space that represents very limited reactant mobility, second, the higher $p(O_2)$ accelerates oxide growth rates and opens the Cabrera-Mott regime to direct observation but limits our view of the early oxidation steps. The experimental trade-off is that we worked close to the limits of information depth for XPS, which will be remedied in future work by the use of higher photon energies. The gap in processing conditions, both with respect to $p(O_2)$ and oxidation temperature will be filled in future work.

Mo is incorporated into the oxide layer as Mo(VI), which is enriched at the oxide/gas interface and smaller contributions of Mo(IV) are present throughout the oxide. The rapid Cr-depletion of the alloy seen at higher oxidation temperatures is not replicated and Cr, and Mo, are still present at the alloy/oxide interface—a phenomenon that might be attributed to a diffusion rate mismatch at the interface. The oxide layer is nearly continuous after the first oxidation step as judged by the attenuation of the alloy signal, and we therefore observe the Cabrera-Mott oxidation regime.

In the low-temperature regime probed here, the limiting factor that controls oxide composition is not set anymore by alloy surface chemistry but by the availability of reactants. This is also evident in the comparison of Ni-15Cr, with its unusually low Cr inventory, and the other alloys: the oxide growth is nearly identical when Ni-15Cr and Ni-5Cr are compared and both alloys have nearly the same near-surface alloy composition prior to the oxidation experiment. The oxide composition can therefore be controlled by thermal cycling or other processing protocols that determine near-surface compositions: an oxide layer dominated by chromia can be achieved if the pretreatment of the alloy leads to near-surface Cr-enrichment. The Mo concentration is not affected by the thermal reduction step, and Mo is integrated in the oxide in concentrations similar to the bulk.[37]

The Supplemental Material includes STM images of oxide islands recorded after oxidation of a Ni-10Cr-6Mo(100) surface at 300°C which illustrate the relatively poor crystallinity of the oxide islands through the combined action of limited reactant diffusion and a short oxygen capture radius (Supplemental Material Figure S3).[37] The significant concentration of defects, at least at the island perimeter, seems on first sight to contradict the low concentration of Ni^{3+} defects cited in Figure 4. However, the defect inventory is most certainly much more diverse and numerous types of defects are present which are not captured in XPS, and the Ni^{3+} concentration is measured for much thicker oxide layers. A direct quantitative comparison is therefore not valid.

We propose that elemental reaction steps in the surface chemistry are suppressed: while O_{ads} depends only on the local adsorption sites on the alloy, the nucleation and sustained growth of chromia requires the diffusion of Cr atoms. At higher temperatures, chromia nucleation and growth proceed in all likelihood close to the primary oxygen adsorption sites: Cr-W-O or Cr-Mo-O. At 200°C, on the other hand, the severely limited surface diffusion of Cr (and Mo) removes the benefit of the Cr-Mo-O site to favor chromia over NiO. As a consequence, the oxide composition only depends on the local environment at the alloy surface and scales with near-surface alloy composition. The computational description of MAE effects therefore has to include an additional descriptor that relates to surface and near-surface diffusion coefficients.

CONCLUSIONS

➢ In the regime of very limited diffusion the near-surface composition of the alloys is imprinted on the oxide. Alloy processing prior to oxidation can be used to modulate the near-surface composition and, in our work, vacuum annealing removed the native oxide resulting in a pristine alloy surface. Even for variable bulk composition shown in the comparison of Ni-5Cr and Ni-15Cr, a near identical near-surface composition can be reached and determines chromia content in the oxide as seen in Figure 8. Cr enrichment in the near-surface region triggered by processing (annealing) is particularly high for Ni-15Cr-6Mo; an observation also made in prior work for Ni-Cr-W alloys and attributed to accelerated diffusion and segregation of Cr at the surface of the ternary alloy. Experimental evidence from our work supports these ideas, but a quantitative study of diffusion coefficients and paths is still necessary for confirmation. Hence, the near-surface composition in the alloy is reflected in the oxide layer and surface chemistry becomes of minor importance in this regime. As a consequence, alloy processing that favors a near-surface Cr-enrichment can be used to seed a chromia-rich oxide layer, and enhance the protective function. On the other hand, we cannot rely on knowledge of the bulk composition to uniquely predict oxide composition and functionality.

ACKNOWLEDGMENTS

We gratefully acknowledge the support of Prof. John Perepezko, University of Wisconsin-Madison, who cast the alloys used in this work. This work was supported by the Office of Naval Research Multi-University Research Initiative "Understanding Atomic Scale Structure in Four Dimensions to Design and Control Corrosion Resistant Alloys" on Grant No. N00014-14-1-0675 under the direction of Dr. David Shifler. Reinke acknowledges the support by NSF DMR Metals and Metallic Nanostructures Award No. 2004326. This research used resources of the 23-ID-2 (IOS) beamline of the National Synchrotron Light Source II, a U.S. Department of Energy (DOE) Office of Science User Facility operated for the DOE Office of Science by Brookhaven National Laboratory under Contract No. DE-SC0012704. The support for V.A.A. to conduct this work by Prof. E. Opila (UVa) is gratefully acknowledged. The experimental data from this report will be made available if a reasonable request is made to the corresponding author.

AUTHOR CONTRIBUTIONS

G.R. and V.A.A. performed the experiments with the guidance of I.W. and A.H. The data analysis was performed by C.V., G.R., and P.R. The results were discussed by all authors. P.R. and C.V. wrote the manuscript which was proofread and approved for submission by all authors. P.R. conceived and led the study.

DECLARATION OF COMPETING INTEREST

The authors declare no competing financial interest.

References

1. A.P. Bond, H.H. Uhlig, *J. Electrochem. Soc.* 107 (1960): p. 488.
2. B. Chattopadhyay, G.C. Wood, *Oxid. Met.* 2 (1970): p. 373-399.
3. G.C. Wood, B. Chattopadhyay, *Corros. Sci.* 10 (1970): p. 471-480.
4. G.C. Wood, T. Hodgkiess, *Nature* 211 (1966): p. 1358-1361.
5. R.M. Carranza, M.A. Rodríguez, *npj Mater. Degrad.* 1 (2017): p. 9.
6. R.S. Lillard, M.P. Jurinski, J.R. Scully, *Corrosion* 50 (1994): p. 251-265.
7. T.M. Pollock, S. Tin, *J. Propulsion Power* 22 (2006): p. 361-374.
8. A.C. Lloyd, J.J. Noël, S. McIntyre, D.W. Shoesmith, *Electrochim. Acta* 49 (2004): p. 3015-3027.
9. F. Bocher, R. Huang, J.R. Scully, *Corrosion* 66 (2010): p. 055002-055001-055002-055015.
10. F. Bocher, R. Huang, J.R. Scully, *Corrosion* 66 (2010): p. 055002-055002-055015.
11. N. Ebrahimi, M.C. Biesinger, D.W. Shoesmith, J.J. Noël, *Surf. Interface Anal.* 49 (2017): p. 1359-1365.
12. J.R. Hayes, J.J. Gray, A.W. Szmodis, C.A. Orme, *Corrosion* 62 (2006): p. 491-500.
13. K. Lutton Cwalina, C.R. Demarest, A.Y. Gerard, J.R. Scully, *Curr. Opin. Solid State Mater. Sci.* 23 (2019): p. 129-141.
14. M. Urquidi, D.D. Macdonald, *J. Electrochem. Soc.* 132 (1985): p. 555-558.
15. K. Gusieva, K.L. Cwalina, W.H. Blades, G. Ramalingam, J.H. Perepezko, P. Reinke, J.R. Scully, *J. Phys. Chem. C* 122 (2018): p. 19499-19513.
16. L.F. Lin, C.Y. Chao, D.D. Macdonald, *J. Electrochem. Soc.* 128 (1981): p. 1194-1198.
17. C.T. Liu, J. Ma, X.F. Sun, *J. Alloys Compd.* 491 (2010): p. 522-526.
18. N. Hussain, K.A. Shahid, I.H. Khan, S. Rahman, *Oxid. Met.* 41 (1994): p. 251-269.
19. F.A. Khalid, N. Hussain, K.A. Shahid, *Mater. Sci. Eng. A* 265 (1999): p. 87-94.
20. W.H. Blades, M.R. Barone, P. Reinke, *npj Mater. Degrad.* 5 (2012): p. 1-10.
21. W.H. Blades, P. Reinke, *ACS Appl. Mater. Interfaces* 10 (2018): p. 43219-43229.
22. C. Volders, V.A. Angelici, I. Waluyo, A. Hunt, L. Árnadóttir, P. Reinke, *npj Mater. Degrad.* 6 (2022): p. 52.
23. L. Ma, F. Wiame, V. Maurice, P. Marcus, *Corros. Sci.* 140 (2018): p. 205-216.
24. V. Maurice, G. Despert, S. Zanna, M.P. Bacos, P. Marcus, *Nat. Mater.* 3 (2004): p. 687-691.
25. V. Maurice, P. Marcus, *Prog. Mater. Sci.* 95 (2018): p. 132-171.
26. X.-X. Yu, A. Gulec, C.M. Andolina, E.J. Zeitchick, K. Gusieva, J.C. Yang, J.R. Scully, J.H. Perepezko, L.D. Marks, *Corrosion* 74 (2018): p. 939-946.
27. L. Luo, L. Zou, D.K. Schreiber, D.R. Baer, S.M. Bruemmer, G. Zhou, C.-M. Wang, *Scr. Mater.* 114 (2016): p. 129-132.
28. L. Ma, F. Wiame, V. Maurice, P. Marcus, *npj Mater. Degrad.* 3 (2019): p. 29.
29. A.J. Samin, C.D. Taylor, *Corros. Sci.* 134 (2018): p. 103-111.
30. T.D. Doležal, A.J. Samin, *Langmuir* 38 (2022): p. 3158-3169.
31. A.P. Greeff, C.W. Louw, H.C. Swart, *Corros. Sci.* 42 (2000): p. 1725-1740.
32. H.J. Mathieu, D. Landolt, *Corros. Sci.* 26 (1986): p. 547-559.
33. M.F. Montemor, A.M.P. Simões, M.G.S. Ferreira, M.D.C. Belo, *Corros. Sci.* 41 (1999): p. 17-34.
34. C.E. Campbell, W.J. Boettinger, U.R. Kattner, *Acta Mater.* 50 (2002): p. 775-792.
35. T. Gheno, F. Jomard, C. Desgranges, L. Martinelli, *Materialia* 3 (2018): p. 145-152.
36. J.D. Tucker, R. Najafabadi, T.R. Allen, D. Morgan, *J. Nucl. Mater.* 405 (2010): p. 216-234.
37. R. Ramanathan, G. Ramalingam, J.H. Perepezko, P. Reinke, P.W. Voorhees, *ACS Appl. Mater. Interfaces* 10 (2018): p. 9136-9146.
38. H. Liu, Z. Lin, L.V. Zhigilei, P. Reinke, *J. Phys. Chem. C* 112 (2008): p. 4687-4695.
39. I. Waluyo, A. Hunt, *Synchrotron Radiat. News* 35 (2022): p. 31-38.
40. D. Berztiss, R. Cerchiara, E. Gulbransen, F. Pettit, G. Meier, *Mater. Sci. Eng. A* 155 (1992): p. 165-181.
41. M.C. Biesinger, C. Brown, J.R. Mycroft, R.D. Davidson, N.S. McIntyre, *Surf. Interface Anal.* 36 (2004): p. 1550-1563.
42. M.C. Biesinger, B.P. Payne, A.P. Grosvenor, L.W.M. Lau, A.R. Gerson, R.S.C. Smart, *Appl. Surf. Sci.* 257 (2011): p. 2717-2730.
43. M.C. Biesinger, B.P. Payne, L.W.M. Lau, A. Gerson, R.S.C. Smart, *Surf. Interface Anal.* 41 (2009): p. 324-332.
44. B.P. Payne, M.C. Biesinger, N.S. McIntyre, *J. Electron Spectrosc. Relat. Phenom.* 184 (2011): p. 29-37.
45. B.P. Payne, A.P. Grosvenor, M.C. Biesinger, B.A. Kobe, N.S. McIntyre, *Surf. Interface Anal.* 39 (2007): p. 582-592.
46. S. Doniach, M. Sunjic, *J. Phys. C* 3 (1970): p. 285-291.
47. J.H. Scofield, *J. Electron Spectrosc. Relat. Phenom.* 8 (1976): p. 129-137.
48. S.-P. Jeng, P.H. Holloway, C.D. Batich, *Surf. Sci.* 193 (1988): p. L63-L68.
49. A.V. Ruhan, H.L. Skriver, J.K. Norskov, *Phys. Rev. B* 59 (1999): p. 15990-16000.
50. Y. Yu, W. Xiao, J. Wang, L. Wang, *Materials (Basel)* 9 (2015): p. 5-15.
51. M. Bohra, P. Grammatikopoulos, R.E. Diaz, V. Singh, J. Zhao, J.-F. Bobo, A. Kuronen, F. Djurabekova, K. Nordlund, M. Sowwan, *Chem. Mater.* 27 (2015): p. 3216-3225.
52. J.C. Yang, M. Yeadon, D. Olynick, J.M. Gibson, *Microsc. Microanal.* 3 (1997): p. 121-125.
53. J. Yeh, I. Lindau, *Atomic Data Nucl. Data Tables* 32 (1985): p. 1-155.
54. B. Cabrera, N.F. Mott, *Rep. Prog. Phys.* 12 (1949): p. 163-185.
55. N. Zhu, J. Li, X.-G. Lu, Y. He, J. Zhang, *Metall. Mater. Trans. A* 46 (2015): p. 5444-5455.
56. K.S. Kim, R.E. Davis, *J. Electron Spectrosc. Relat. Phenom.* 1 (1972): p. 251-258.
57. A.P. Grosvenor, M.C. Biesinger, R.S.C. Smart, N.S. McIntyre, *Surf. Sci.* 600 (2006): p. 1771-1779.
58. J. Dereń, J. Stoch, *J. Catal.* 18 (1970): p. 249-259.
59. A.F. Carley, S.D. Jackson, J.N. O'Shea, M.W. Roberts, *Surf. Sci. Lett.* 440 (1999): p. L868-L874.
60. P.C. Gravelle, S.J. Teichner 20 (1969): p. 167-266.
61. G. Ma, X. Tang, Z. Zhong, H. Zhang, H. Su, *Microelectron. Eng.* 108 (2013): p. 8-10.
62. J.M. McKay, V.E. Henrich, *Phys. Rev. B* 32 (1985): p. 6764-6772.

63. L.M. Moroney, R.S.C. Smart, M.W. Roberts, *J. Chem. Soc., Faraday Trans.* 1 79 (1983): p. 1769-1778.
64. B.P. Payne, M.C. Biesinger, N.S. McIntyre, *J. Electron Spectrosc. Relat. Phenom.* 185 (2012): p. 159-166.
65. M.W. Roberts, R.S.C. Smart, *J. Chem. Soc., Faraday Trans.* 1 80 (1984): p. 2957-2968.
66. D. Soo Kim, H. Chul Lee, *J. Appl. Phys.* 112 (2012).
67. G. Tyuliev, M. Sokolova, *Appl. Surf. Sci.* 52 (1991): p. 343-349.
68. S. Uhlenbrock, C. Scharfschwerdt, N. Neumann, G. Illing, H.-J. Freund, *J. Phys. Condens. Matter* 4 (1992): p. 7973-7978.
69. J.-L. Yang, Y.-S. Lai, J.S. Chen, *Thin Solid Films* 488 (2005): p. 242-246.
70. D. Yue, C. Guo, X. Yan, R. Wang, M. Fang, Y. Wu, X. Qian, Y. Zhao, *Chem. Eng. J.* 360 (2019): p. 97-103.
71. S. Tanuma, C.J. Powell, D.R. Penn, *Surf. Interface Anal.* 21 (1994): p. 165-176.
72. A. Larsson, G. D'Acunto, M. Vorobyova, G. Abbondanza, U. Lienert, Z. Hegedüs, A. Preobrajenski, L.R. Merte, J. Eidhagen, A. Delblanc, *J. Alloys Compd.* 895 (2022): p. 162657.
73. J.E. Castle, K. Asami, *Surf. Interface Anal.* 36 (2004): p. 220-224.
74. Y. Unutulmazsoy, R. Merkle, D. Fischer, J. Mannhart, J. Maier, *Phys. Chem. Chem. Phys.* 19 (2017): p. 9045-9052.
75. C.E. Campbell, W.J. Boettinger, U.R. Kattner, *Acta Mater.* 50 (2002): p. 775-792.
76. Y. Xie, D.M. Artymowicz, P.P. Lopes, A. Aiello, D. Wang, J.L. Hart, E. Anber, M.L. Taheri, H. Zhuang, R.C. Newman, K. Sieradzki, *Nat. Mater.* 20 (2021): p. 789-793.
77. H. Ke, C.D. Taylor, *J. Electrochem. Soc.* 167 (2020).
78. O. Olatunji-Ojo, C.D. Taylor, *Philos. Mag.* 93 (2013): p. 4286-4310.
79. N.K. Das, T. Shoji, *App. Surf. Sci.* 445 (2018): p. 217-228.